FEM-DDM WITH AN EFFICIENT SECOND-ORDER TRANSMISSION CONDITION IN BOTH HIGH-FREQUENCY AND LOW-FREQUENCY APPLICATIONS

Jin Ma[1, 2, *] and Zaiping Nie[1, 3]

[1]Department of Electronic Engineering, University of Electronic Science and Technology of China, Chengdu, Sichuan 610054, China

[2]Department of Electrical and Computer Engineering, University of Illinois at Urbana-Champaign, Urbana, IL 61801-2991, USA

[3]Department of Microwave Engineering, University of Electronic Science and Technology of China, Chengdu, Sichuan 610054, China

Abstract—In this paper, a novel second-order transmission condition is developed in the framework of non-conformal finite element domain decomposition method to meet the challenges brought by complex and large-scale electromagnetic modeling. First, it is implemented efficiently on the non-conformal interface via a Gauss integral scheme. Then, the eigenvalue analysis of the DDM system show a more clustered eigenvalue distribution of this transmission condition compared with several existing transmission conditions. After that, it is applied to large-scale complex problems such as S-type waveguides in the high frequency band and dielectric well-logging applications in the low frequency band. The final numerical results demonstrate that this transmission condition has high efficiency and huge capability for modeling large-scale problems with multi-resolution in any frequency band.

1. INTRODUCTION

In numerical modeling of electromagnetic (EM) problems, the solution domain of practical concerns usually consist of sensors, antenna arrays, or propagating structures with complex details. Traditional numerical methods, such as the finite element method (FEM) [16, 17, 19, 20],

which is adaptive to the arbitrary-shaped problems, are now challenged by the problems such as excessive memory cost, long computation time, and limited modeling capability. However, based on the idea of Schwartz Method and Lagrange Multiplier, these methods such as FEM are now combined with a more efficient domain decomposition method (DDM) [1–15]. Under this domain decomposition framework, large-scale EM problems can now be modeled with high parallel efficiency, especially with the aid of improved transmission conditions (TCs) at subdomain interfaces.

At first, when Schwartz Method is introduced to the EM numerical modeling, Dirichlet boundary condition and Neumann boundary condition are used to couple fields between different subdomains. This is well known as FETI-DP method. Then, in order to overcome some convergence problems in FETI-DP and make domain decomposition more flexible, Lagrange Multiplier was introduced to combine these boundary conditions together to form transmission conditions between subdomains. These transmission conditions can have a better convergence and modeling flexibility, while they can still keep the original continuity of electromagnetic fields at interface between different subdomains. In the past, there are several transmission conditions implemented in DDM in the EM area. At the beginning, the first-order transmission condition (FOTC) is invented such as the Robin-type transmission condition. This Robin-type transmission condition has a good convergence performance when there is only propagating mode involved on the interfaces [1–7]. However, it is reported later that when there is TE or TM evanescent mode on the interface, the convergence of this FOTC becomes poor and a second-order TC (SOTC) which could successfully converge with TE evanescent mode on the interface is implemented [9, 12]. And later on, an SOTC which could perform well with both TE and TM evanescent modes on the interface has been well developed [13, 14]. The progress of these TCs can be concluded mathematically from their eigenvalue distributions. Each time a better TC is developed, its eigenvalue distribution becomes more clustered in the center of the unit circle. In this paper, a novel SOTC is derived and then compared with the aforementioned TCs. The comparison is done by analyzing the eigenvalue distribution and the iterative convergence with both normal mesh size and extremely dense mesh size to mimic the high-frequency and low-frequency applications. The results of the eigenvalue distribution illustrate that the SOTC derived in this paper has a more clustered eigenvalue distribution. To extend its implementation in the non-conformal finite-element-based domain decomposition method (NC-FEM-DDM), Lagrange interpolation is introduced to realize the

Gauss integral on the non-conformal interface, which is evidently more efficient compared with the treatments of integral on the interface before.

Finally, the proposed SOTC in NC-FEM-DDM is applied to model an S-type waveguide with complex propagating structures in the high-frequency band and a dielectric well-logging tool with complex sensor arrays in the low-frequency band. The modeling results not only demonstrate a remarkable agreement of the method with other methods, but also show highly efficiency of our proposed TC compared with other TCs.

2. NON-CONFORMAL FEM-DDM WITH TRANSMISSION CONDITIONS

2.1. Formulation of NC-FEM-DDM with Transmission Conditions

For EM problems with interior sources and truncated boundaries, applying the testing function to the vector wave equation and transferring the first curl to the testing function yields

$$\left\langle \nabla \times \mathbf{W}_i, \mu_{ri}^{-1} \nabla \times \mathbf{E}_i \right\rangle_v - k_0^2 \langle \mathbf{W}_i, \varepsilon_{ri}\mathbf{E}_i \rangle_v + k_i \langle \mathbf{W}_i, \mathbf{j}_i \rangle_s$$
$$= -j\omega\mu_0 \langle \mathbf{W}_i, \mathbf{J}_i^{\text{inc}} \rangle_v \tag{1}$$

where $\langle \mathbf{a}, \mathbf{b} \rangle_v$ denotes the volume integration of the scalar product between $\mathbf{a}$ and $\mathbf{b}$, and $\langle \mathbf{a}, \mathbf{b} \rangle_s$ denotes the surface integration of the scalar product between $\mathbf{a}$ and $\mathbf{b}$. $\mathbf{W}_i$ is the testing function, $\mathbf{E}_i$ the electric field in domain i, $\mathbf{j}_i$ the auxiliary current on the interface of domain i, and $\mathbf{J}_i^{\text{inc}}$ the excitation source inside domain i.

The transmission conditions are used to couple the fields between subdomains. In this paper, we first review three commonly used TCs for DDM. They are summarized as follows.

The first-order TC (FOTC) is expressed as

$$k_{ij}\mathbf{j}_i + \alpha\mathbf{e}_i = -k_{ij}\mathbf{j}_j + \alpha\mathbf{e}_j \quad \text{on} \quad \partial S_{ij} \tag{2}$$

and the second-order TC for TE evanescent mode (SOTC-TE) [12] is expressed as

$$k_{ij}\mathbf{j}_i + \alpha\mathbf{e}_i + \beta\nabla_t \times \nabla_t \times \mathbf{e}_i = -k_{ij}\mathbf{j}_j + \alpha\mathbf{e}_j + \beta\nabla_t \times \nabla_t \times \mathbf{e}_j \quad \text{on} \quad \partial S_{ij} \tag{3}$$

whereas the second-order TC for both TE and TM evanescent mode (SOTC-Full) [14] is expressed as

$$k_{ij}\mathbf{j}_i + \alpha\mathbf{e}_i + \beta\nabla_t \times \nabla_t \times \mathbf{e}_i + \gamma\nabla_t p_i$$
$$= -k_{ij}\mathbf{j}_j + \alpha\mathbf{e}_j + \beta\nabla_t \times \nabla_t \times \mathbf{e}_j - \gamma\nabla_t p_j \quad \text{on} \quad \partial S_{ij}. \tag{4}$$

Here $k_{ij} = k_0 \sqrt{\mu_{rij} \varepsilon_{rij}}$, $\mu_{rij} = \sqrt{\mu_{ri} \mu_{rj}}$,   and $\varepsilon_{rij} = \sqrt{\varepsilon_{ri} \varepsilon_{rj}}$,
and the variables used in these equations are defined as follows

$$\mathbf{j}_i = \frac{1}{k_i} \mathbf{n}_i \times \left(\mu_{ri}^{-1} \nabla \times \mathbf{E}_i \right) \tag{5}$$

$$\mathbf{e}_i = \mathbf{n}_i \times \mathbf{E}_i \times \mathbf{n}_i. \tag{6}$$

$$p_i = \frac{1}{k_i} \nabla_t \cdot \mathbf{j}_i \tag{7}$$

$$\text{or} \quad p_i = -E_i^n \tag{8}$$

where E_i^n denotes the normal component of the electric field on the interface. The tangential field $\mathbf{e}_i$ can be expanded using the existing curl-conforming basis function $\mathbf{W}_k$ for electric field $\mathbf{E}_i$, while the surface current $\mathbf{j}_i$ can be expanded as follows

$$\mathbf{j}_i = \sum_k \mathbf{S}_k J_k \tag{9}$$

where $\mathbf{S}_k$ is the basis function for the current, which may be derived from the curl-conforming basis function $\mathbf{W}_k$

$$\mathbf{S}_k = \mathbf{n} \times (\nabla \times \mathbf{W}_k) \tag{10}$$

$$\text{or} \quad \mathbf{S}_k = \mathbf{n} \times (\mathbf{W}_k) \tag{11}$$

$$\text{or} \quad \mathbf{S}_k = \mathbf{W}_k \tag{12}$$

It is recommended that a divergence-conforming basis function such as RWG or Eq. (11) should be used to expand the current in the integral equation method. However, the curl-conforming basis functions such as Eq. (10) and Eq. (12) would make the eigenvalue distribution of the DDM system more clustered. As a result, Eq. (10) or Eq. (12) is usually chosen to expand the surface current $\mathbf{j}_i$ in a domain decomposition method.

Finally, the auxiliary variable p_i can be expanded as follows

$$p = \sum_k \phi_k P_k \tag{13}$$

where

$$\phi_k = \frac{1}{8} (1 + u_k u)(1 + v_k v)(1 + w_k w). \tag{14}$$

In Eq. (14), (u, v, w) is the local coordinate of a unit cube transferred from an arbitrary hexahedral element via Jacobi transform. From Eq. (14) we can see that the second-order term $\nabla_t p_i$ in Eq. (4) can be easily calculated as well.

Equation (8) can be derived from (7) by noting that

$$\nabla_t \cdot \mathbf{j}_i = (\nabla - \nabla_n) \cdot \mathbf{j}_i.$$

Since $\mathbf{j}_i$ has only a tangential component and ∇_n has only a normal component, their scalar product vanishes: hence

$$(\nabla - \nabla_n) \cdot \mathbf{j}_i = \nabla \cdot \mathbf{j}_i.$$

Expanding $\mathbf{j}_i$ using (5) and invoking the vector identity, we obtain

$$\nabla_t \cdot \mathbf{j}_i = \nabla \cdot \mathbf{j}_i = \frac{1}{k_i} \nabla \cdot [\mathbf{n}_i \times (\nabla \times \mathbf{E}_i)] = -\frac{1}{k_i} \mathbf{n}_i \cdot (\nabla \times \nabla \times \mathbf{E}_i).$$

Assuming that on the interface there is no excitation source, the vector wave equation can be written as

$$\nabla \times \nabla \times \mathbf{E}_i - k_i^2 \mathbf{E}_i + k_i \mathbf{j}_i = 0.$$

Again, since $\mathbf{j}_i$ has only tangential component, we finally obtain

$$\nabla_t \cdot \mathbf{j}_i = -\frac{1}{k_i} \mathbf{n}_i \cdot \left(k_i^2 \mathbf{E}_i - k_i \mathbf{j}_i \right) = -k_i E_i^n.$$

The expression in (8) derived in this paper has a clearer physical meaning compared with (7) because the normal component of the electric field has taken place of the divergence of the auxiliary current $\mathbf{j}_i$. Moreover, (8) can be implemented in a straightforward manner by using the components of the electric field normal to the interface. As it is illustrated later, the second-order TC using (8) has a more clustered eigenvalue distribution and consequently the resulting DDM has a better iterative convergence. Since p_i has two forms as shown in (7) and (8), SOTC-Full in (4) can be expressed as SOTC-Full-J by using (7) and SOTC-Full-En if (8) is used instead If the value of complex coefficients α, β, and γ are restricted within a certain range, the continuity for both the electric and the magnetic fields on the interface can be guaranteed. Here, $\alpha = -jk$, while the expressions for β and γ are given in [14].

If we use $k_{ij}\mathbf{j}_i$ to test (4), we will obtain

$$k_{ij}^2 \langle \mathbf{j}_i, \mathbf{j}_i \rangle + \alpha k_{ij} \langle \mathbf{j}_i, \mathbf{e}_i \rangle + \beta k_{ij} \langle \nabla_t \times \mathbf{j}_i, \nabla_t \times \mathbf{e}_i \rangle + \gamma k_{ij} \langle \mathbf{j}_i, \nabla_t p_i \rangle$$
$$= -k_{ij}^2 \langle \mathbf{j}_i, \mathbf{j}_j \rangle + \alpha k_{ij} \langle \mathbf{j}_i, \mathbf{e}_j \rangle$$
$$+ \beta k_{ij} \langle \nabla_t \times \mathbf{j}_i, \nabla_t \times \mathbf{e}_j \rangle - \gamma k_{ij} \langle \mathbf{j}_i, \nabla_t p_j \rangle. \tag{15}$$

Multiply (15) with coefficient $k_i / \alpha k_{ij}$ and results in

$$k_{ij} k_i / \alpha \langle \mathbf{j}_i, \mathbf{j}_i \rangle + k_i \langle \mathbf{j}_i, \mathbf{e}_i \rangle$$
$$+ \beta k_i / \alpha \langle \nabla_t \times \mathbf{j}_i, \nabla_t \times \mathbf{e}_i \rangle + \gamma k_i / \alpha \langle \mathbf{j}_i, \nabla_t p_i \rangle$$
$$= -k_{ij} k_i / \alpha \langle \mathbf{j}_i, \mathbf{j}_j \rangle + k_i \langle \mathbf{j}_i, \mathbf{e}_j \rangle$$
$$+ \beta k_i / \alpha \langle \nabla_t \times \mathbf{j}_i, \nabla_t \times \mathbf{e}_j \rangle - \gamma k_i / \alpha \langle \mathbf{j}_i, \nabla_t p_j \rangle. \tag{16}$$

If we use p_i to test (8), we will obtain

$$\langle p_i, p_i \rangle + \langle p_i, E_i^n \rangle = 0. \tag{17}$$

Combine (1), (16) and (17), we can get the final quasi-symmetry functional matrix for domain i:

$$
\left(
\begin{bmatrix} A_i & C_i & 0 & 0 \\ C_i & B_i & D_i & 0 \\ 0 & D_i & T_i & 0 \\ 0 & 0 & 0 & P_i \end{bmatrix}
+
\begin{bmatrix} 0 & 0 & 0 & 0 \\ 0 & 0 & 0 & 0 \\ 0 & D_i^{'} & 0 & TP_i \\ TE_i^n & 0 & 0 & 0 \end{bmatrix}
\right)
\begin{bmatrix} E_i \\ E_{Bi} \\ J_i \\ P_i \end{bmatrix}
$$

$$
=
\begin{bmatrix} F_i \\ 0 \\ 0 \\ 0 \end{bmatrix}
+
\begin{bmatrix} 0 & 0 & 0 & 0 \\ 0 & 0 & 0 & 0 \\ 0 & TB_{ij} & TT_{ij} & TP_{ij} \\ 0 & 0 & 0 & 0 \end{bmatrix}
\begin{bmatrix} E_j \\ E_{Bj} \\ J_j \\ P_j \end{bmatrix}.
\tag{18}
$$

In (18), matrix $\begin{bmatrix} A_i & C_i \\ C_i & B_i \end{bmatrix}$ represents the original functional matrix derived from vector wave Eq. (1), while

$$
D_i = k_i \langle \mathbf{e}_i, \mathbf{j}_i \rangle
\tag{19}
$$

$$
D_i^{'} = \beta k_i / \alpha \langle \nabla_t \times \mathbf{j}_i, \nabla_t \times \mathbf{e}_i \rangle
\tag{20}
$$

$$
T_i = k_{ij} k_i / \alpha \langle \mathbf{j}_i, \mathbf{j}_i \rangle
\tag{21}
$$

$$
P_i = k_i \langle p_i, p_i \rangle
\tag{22}
$$

$$
TP_i = -\gamma \langle \mathbf{j}_i, \nabla_t p_i \rangle
\tag{23}
$$

$$
TE_i^n = \langle p_i, E_i^n \rangle
\tag{24}
$$

$$
TB_{ij} = k_i \langle \mathbf{j}_i, \mathbf{e}_j \rangle + \beta k_i / \alpha \langle \nabla_t \times \mathbf{j}_i, \nabla_t \times \mathbf{e}_j \rangle
\tag{25}
$$

$$
TT_{ij} = -k_{ij} k_i / \alpha \langle \mathbf{j}_i, \mathbf{j}_j \rangle
\tag{26}
$$

$$
TP_{ij} = -\gamma k_i / \alpha \langle \mathbf{j}_i, \nabla_t p_j \rangle.
\tag{27}
$$

The matrix on the left side of Eq. (18) is segmented in to two parts so that the major calculation on the symmetrical matrix can be saved by half. Eqs. (25), (26) and (27) have to be calculated on the non-conformal interface. In Part B, an efficient Gaussian integration on the non-conformal interface will be introduced.

2.2. Gauss Integral on the Non-conformal Interface

There are few papers discussing about the integration on the non-conformal interface when terms in (25)–(27) need to be calculated, in which the basic functions for variables such as $\mathbf{j}_i$ and $\mathbf{e}_j$ are locally defined within different subdomains. It is reported that the treatment of integration on the non-conformal interface is done by recreating a uniform set of mesh cells which would be compatible with the dual-cells on both sides of the interface. As a result, $\mathbf{j}_i$ and $\mathbf{e}_j$ will still share the same Gauss nodes in a smaller cell. However, this process not only suffers from the limitation of its capability on arbitrary shaped
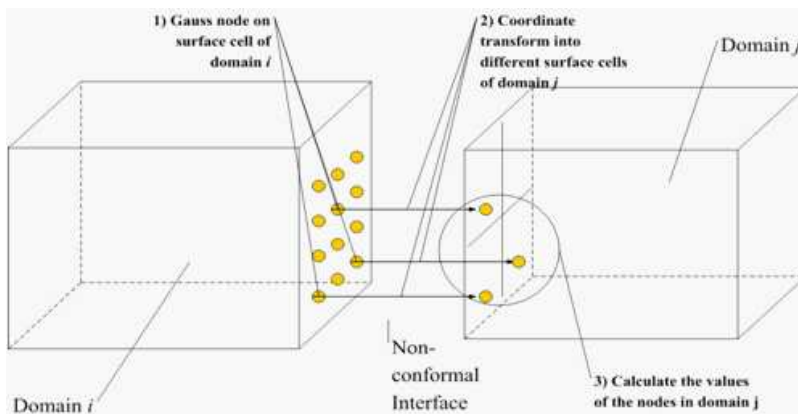
Figure 1. Gauss nodes on non-conformal interface.

interface, but also increases a lot of complexity by geometrical re-meshing and Gauss integration on much more cells. In this paper, we find a more generalized and easier scheme to compute the integration on the interface without special geometrical treatment, as shown in Fig. 1. Use $\langle \mathbf{j}_i, \mathbf{e}_j \rangle$ on surface cell of domain i as an example:

1) Using Jacobi transform, get Gauss node $\mathbf{r}_i(u, v, w)$ on the surface cell;

2) For each Gauss node $\mathbf{r}_i(u, v, w)$, calculate the value of $\mathbf{j}_i(\mathbf{r}_i(u, v, w))$;

3) Transform the local coordinates of Gauss node into global coordinates:

$$\mathbf{r}_i(u, v, w) \quad \underrightarrow{\text{Lagrange interpolation}} \quad \mathbf{r}_i(x, y, z). \qquad (28)$$

Since domain i and domain j share the same global coordinate system:

$$\mathbf{r}_i(x, y, z) \rightarrow \mathbf{r}_j(x, y, z) \qquad (29)$$

we can transform the global coordinates of Gauss node into local coordinate on surface cell of domain j:

$$\mathbf{r}_j(x, y, z) \quad \underrightarrow{\text{Lagrange interpolation}} \quad \mathbf{r}_j(u', v', w'). \qquad (30)$$

4) Calculate the value of $\mathbf{e}_j(\mathbf{r}_j(u', v', w'))$ on surface cell in domain j.

5) Calculate Gauss integration of $\langle \mathbf{j}_i, \mathbf{e}_j \rangle$ on the interface of domain i;

Comparing the above non-conformal scheme with the integral on conformal interface, the only extra time for non-conformal integral

in this process is to transform the coordinate of each Gauss node in Domain i and j in step 3, which only involves Lagrange's interpolation on the surface. This process is obviously more efficient and convenient than the one mentioned before.

3. EIGENVALUE DISTRIBUTIONS WITH DIFFERENT TRANSMISSION CONDITIONS

To show the differences between the FEM-DDMs using FOTC, SOTC-TE, SOTC-Full-J, and SOTC-Full-En for modeling an EM problem, we first consider an air box with mesh size of $\lambda/20$ and the eigenvalue distributions using different TCs are shown in Fig. 2. From Fig. 2, we
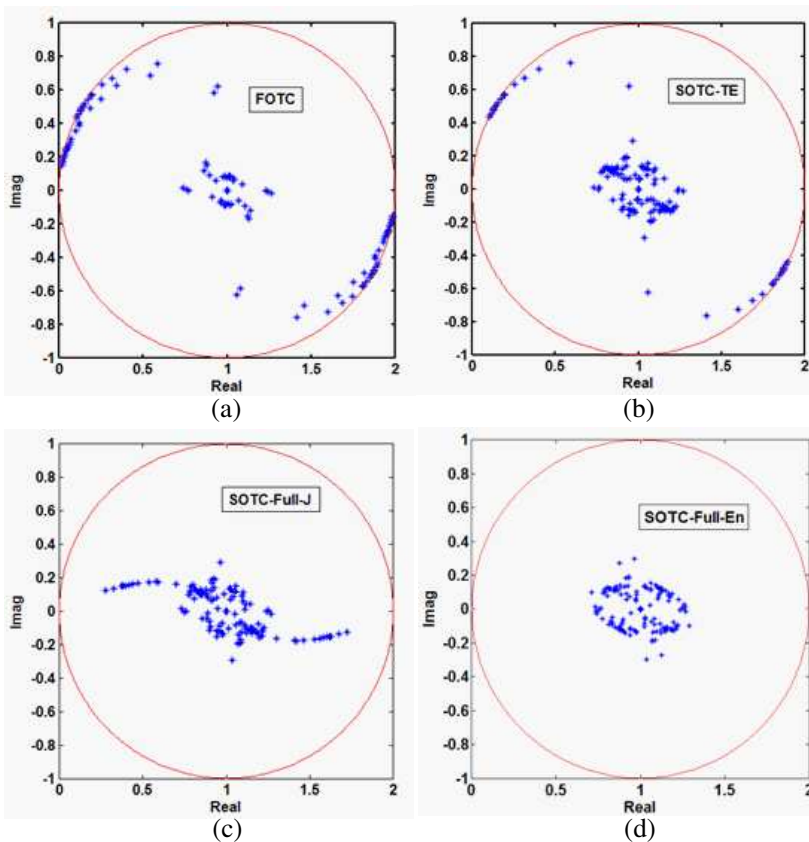
Figure 2. Eigenvalue distributions of the FEM-DDM systems using different TCs with the mesh size of $\lambda/20$. (a) The first-order TC. (b) The second-order TC for TE. (c) The second-order TC-Full using J. (d) The second-order TC-Full using En.

can conclude that the SOTC-Full-En is the best TC among these TCs because all the eigenvalues are clustered near the center of the unit circle.

To mimic the low-frequency application, we decreased the mesh size to $\lambda/3000$. The eigenvalue distributions are shown in Fig. 3. In this case all the eigenvalues are suppressed onto the real axis. It is evident that the best TC is still SOTC-Full-En because of the clustered eigenvalues. The eigenvalues for SOTC-Full-J are also located within the unit circle, however in a complex and mutil-scaled problem, they have more chance to cluster toward the zero eigenvalue and consequently cause near singularity.
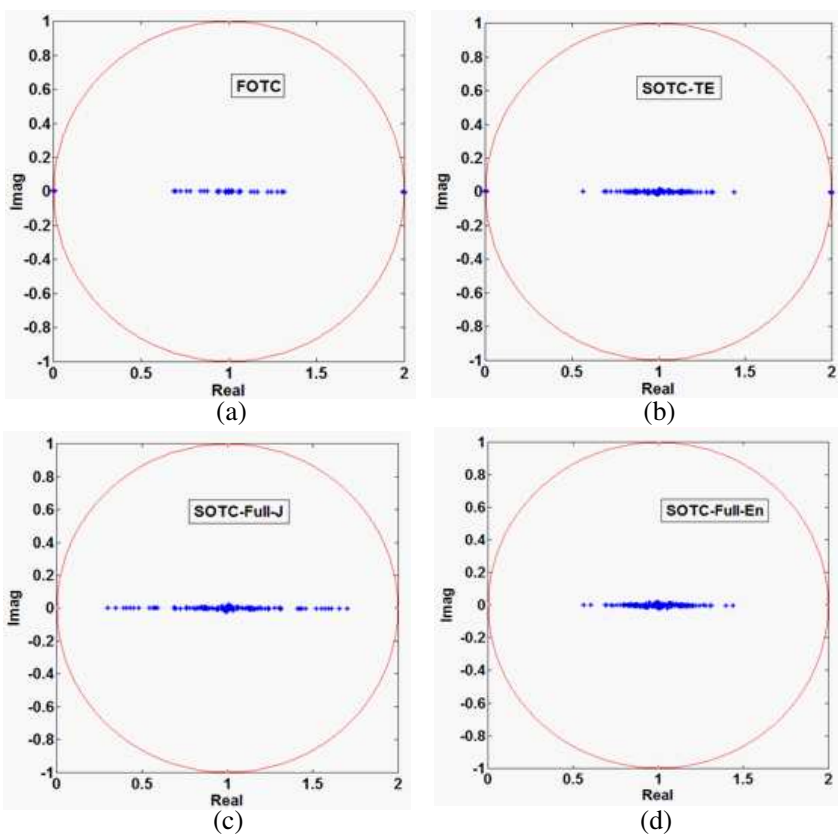
Figure 3. Eigenvalue distributions of the FEM-DDM systems using different TCs with the mesh size of $\lambda/3000$. (a) The first-order TC. (b) The second-order TC for TE. (c) The second-order TC-Full using J. (d) The second-order TC-Full using En.

4. NUMERICAL RESULTS OF COMPLEX WAVEGUIDES AND WELL-LOGGING PROBLEMS

4.1. Modeling of S-type Waveguides in High-frequency Band

In this part, an S-type rectangular waveguide in the high frequency band is taken into consideration as shown in Fig. 4. The parameters in the x- and y-directions of port A are 22.86 mm and 10.16 mm. Assume $z = 0$ mm at port A, the waveguide linearly enlarges its port cross section from $z = 10$ mm to $z = 20$ mm. While the parameters in the x- and y-directions after $z = 20$ mm are 32 mm and 16 mm. The electromagnetic wave will have to pass through a dielectric layer at the end of the S-type waveguide. The parameters of the dielectric layer in the x-, y- and z-directions are 36 mm, 20 mm, and 6 mm. Its relative dielectric constant is 2.25. The working frequency is 10 GHz. The excitation mode is TE_{10} mode with polarization in the y-direction.
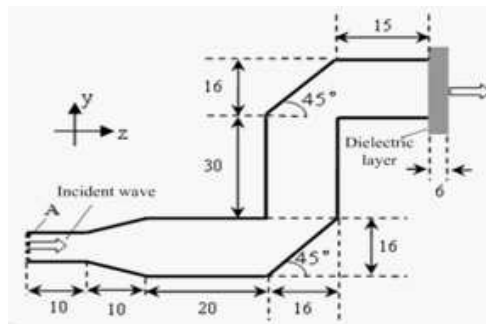
Figure 4. S-type rectangular waveguide.

At first, we will extend the incident port and the output port to illustrate how the wave propagates in the S-type waveguide.

The model and accordingly mesh cells are shown in Fig. 5(a) and the field distribution along the waveguide is shown in Fig. 5(b).

Then we will add the dielectric layer at the end of the port. As can be seen from Fig. 6, the end port of waveguide in Fig. 6(a) stretch into the hole of the structure in Fig. 6(b) and connect with the dielectric layer with a non-conformal interface. The electric field distribution of the YOZ section in this wave guide is compared with FEKO as in Fig. 7, which one can see great agreement of our method with FEKO.

The iterative convergence history of different TCs is given in Fig. 8.

As the convergence history in Fig. 8, SOTC-Full-J and SOTC-Full-En have better iterative convergence than FOTC and SOTC-TE

(a)   (b)
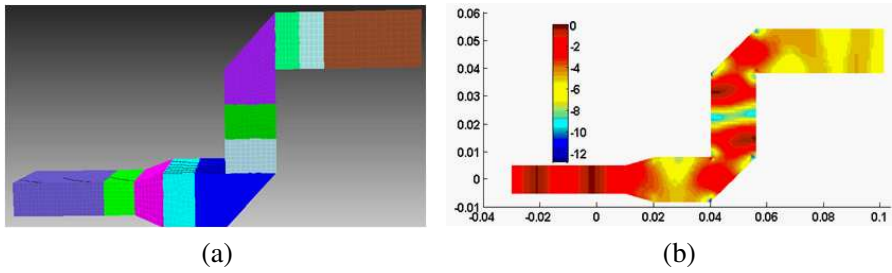
Figure 5. Extended S-type waveguide. (a) Model of the extended S-type waveguide. (b) Field distribution of the extended S-type waveguide.

(a)   (b)
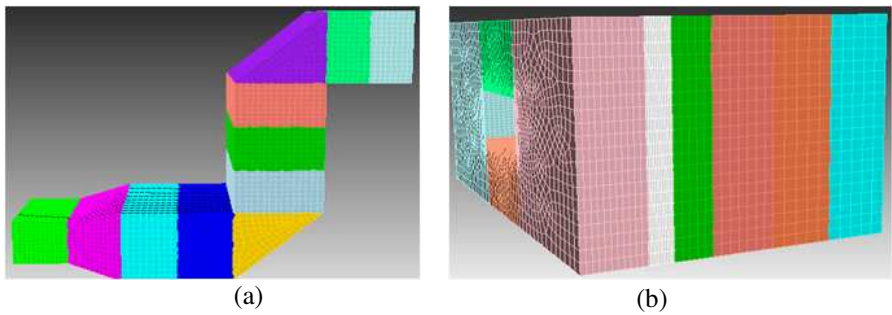
Figure 6. Two independent mesh parts of the S-type waveguide. (a) Waveguide with pure metal structure. (b) Dielectric layer covered by outer air space truncated by absorbing boundary.

(a)   (b)
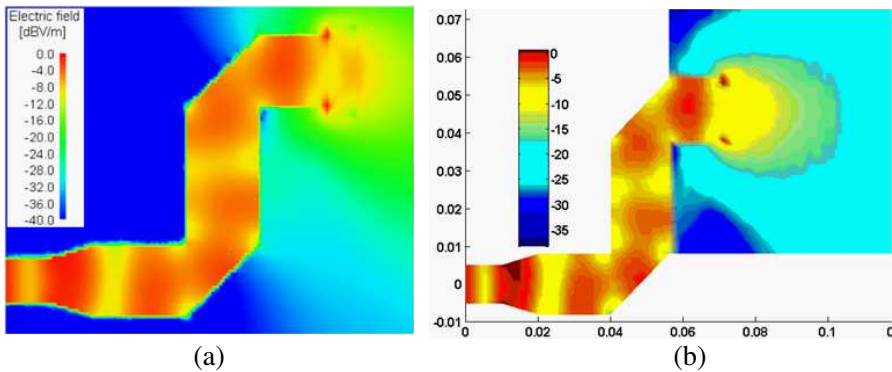
Figure 7. The electric field distribution of the YOZ section. (a) Result by FEKO. (b) Result by non-conformal FEM-DDM.
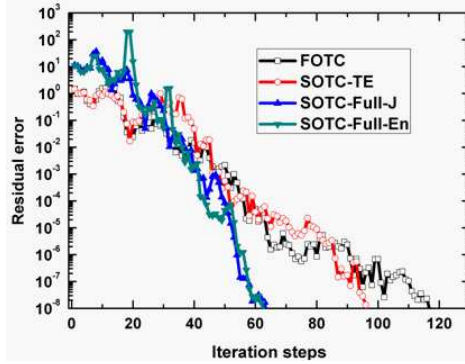
Figure 8. Convergence history of the NC-FEM-DDM using different TCs for the simulation of an S-type rectangular waveguide.

obviously. However, SOTC-Full-En converges with only two steps faster than SOTC-Full-J in this example. The reason is that in the high-frequency band, although the eigenvalue distribution for SOTC-Full-En is more clustered than SOTC-Full-J as illustrated in Fig. 2(c) and Fig. 2(d), the eigenvalue distribution for both SOTC-Full-J and SOTC-Full-En are clustered within the unit circle and there is no eigenvalue clustered towards to the zero eigenvalue yet.

The accuracy loss of DDM compared with FEM is defined as follows:

$$\text{Error} = \left\| \frac{x_{\text{DDM}} - x_{\text{FEM}}}{x_{\text{FEM}}} \right\|_{\max} \tag{31}$$

where x_{DDM} and x_{FEM} are the field distributions at given point calculated by DDM and FEM accordingly.

The accuracy of DDM, the time and memory cost of FEM, DDM

Table 1. Comparison of FEM and NC-FEM-DDM using different transmission conditions.

Step	FEM	DDM-FOTC	SOTC-TE	SOTC-Full-J	SOTC-Full-En
Unknowns	466389	437650	437650	437650	437650
Reading data	245 s	44 s	44 s	44 s	44 s
Geo-assembling	14 s	7 s	7 s	7 s	7 s
Filling Matrix	59 s	19 s	19 s	19 s	19 s
Solving	362 s	241 s	198 s	132 s	129 s
Peak Memory	13.86 GB	6.69 GB	6.69 GB	6.69 GB	6.69 GB
Error	-	0.6×10^{-8}	0.6×10^{-8}	0.6×10^{-8}	0.6×10^{-8}

with FOTC, SOTC-TE, SOTC-Full-J and SOTC-Full-En are given in Table 1.

4.2. Modeling of a Practical Dielectric Tool in Low-frequency Band

To acquire more information and high resolution of the earth, induction well-logging tools developed in recent years are all equipped with large arrays with multi-dimensional coil sensors. An outstanding well-logging tool developed recently is a dielectric scanning tool as illustrated in Fig. 9 [18].
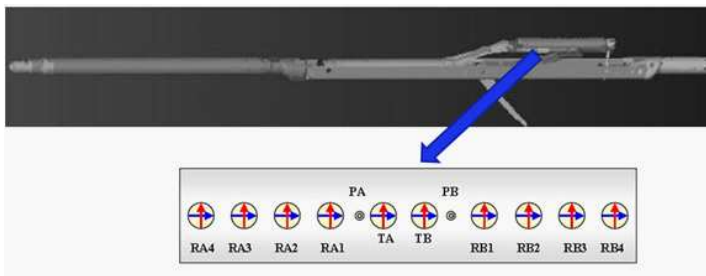
Figure 9. A schematic of the dielectric tool.

In a traditional electromagnetic well-logging application, the conductivity of the object in the earth is the only parameter we concerned because it has major impact on the response at low frequencies. However, this single parameter-interpretation may lead to misreading of the carbonate and heavy oil reservoirs because these reservoirs may be interpreted as surrounding rocks since they share the same high resistivity range. Also the pore-fluid analysis, matrix analysis and geological structure analysis can all be ambiguous as a result of the single parameter- interpretation of the earth. That is why the idea of dielectric tool was brought out in 1980s to get both permittivity and conductivity as the information for the final interpretation.

$$\begin{cases} \varepsilon \\ \sigma \end{cases} \Rightarrow k = \frac{\omega}{c}\sqrt{\mu}\sqrt{\varepsilon_r + j\frac{\sigma}{\omega\varepsilon_0}} \Rightarrow \text{response} \qquad (32)$$

However, the dielectric scanning tool has not been put into practical use until now because of measurement limitations, moderate accuracy and insufficient quality control. As the development in the system design and detecting technology, to model this kind of tool in order to foresee the problems in designing and optimizing parameters becomes

very important and necessary for practical needs. Luckily, the NC-FEM-DDM is developed to solve this kind of problems efficiently. As shown in Fig. 10, since the sensing arrays inside the borehole have small details, fine mesh size is required inside borehole. However, it is not necessary for the layers and objects outside borehole to use the same mesh size. As a result, we divide the original problem into two non-conformal subdomains at the first step: one inside the borehole and the other outside it. The mesh inside the borehole is shown in Fig. 11 and the mesh outside it is shown in Fig. 12. To gain more efficiency and save computational cost, the subdomain inside the borehole is further divided into 2 conformal subdomains and the subdomain outside borehole is further divided into 4 conformal subdomains, which results in totally 6 subdomains.

Considering it works at 20 MHz, the radius of the mandrel is 0.03 m and the radius of the borehole is 0.1524 m, the conductivity inside the borehole is 1×10^{-4} S/m while the conductivity of the layers are 1×10^{-3} S/m. The relative permittivity is set at 1 at first. The electric field distribution at the Z-plane when only one Z-oriented transmitter is excited is shown in Fig. 13. The convergence history for the NC-FEM-DDM with SOTC-Full-En and SOTC-Full-J are shown in Fig. 14. In this example, the NC-FEM-DDM with SOTC-Full-J significantly slows down compared with SOTC-Full-En, which
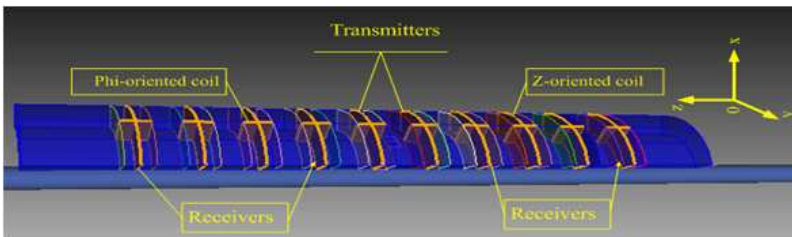
Figure 10. The modeling of the sensing arrays.
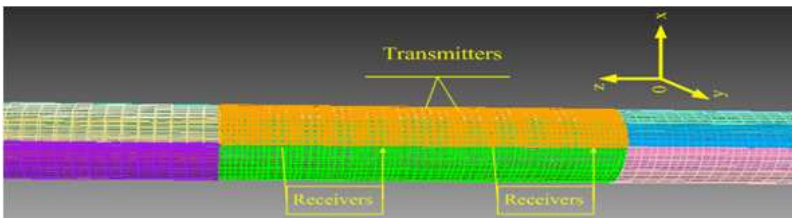
Figure 11. Mesh of the dielectric tool inside borehole.
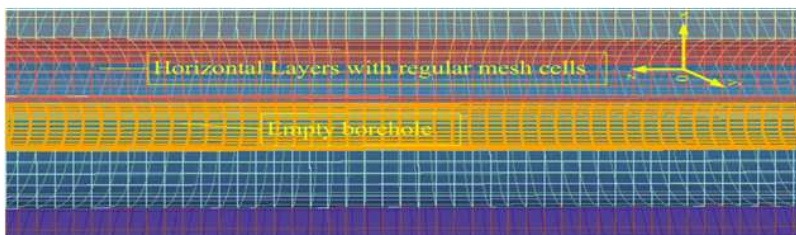
Figure 12. Mesh of the layers outside borehole.
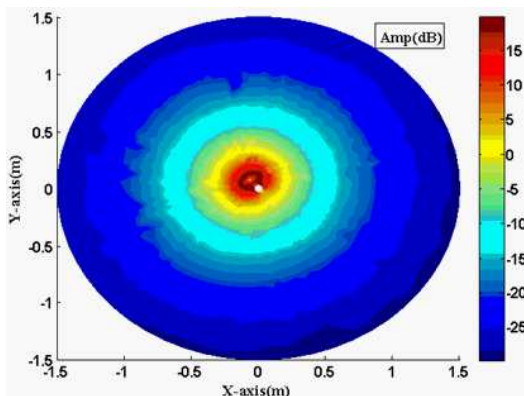
Figure 13. The field distribution at the Z-plane when only one Z-oriented transmitter is excited.

proved our conclusion from the eigenvalue analysis. Since there are some eigenvalues of SOTC-Full-J clustered near the boundary of the unit circle as shown in Fig. 3(c), and there is a possibility that these eigenvalues could be very close to the zero point, which makes the NC-FEM-DDM matrix have near singularity, and consequently suffering from a slow convergence.

Since the iterative convergence is much worse for FOTC and SOTC-TE in this case, we just give the time and memory cost of FEM, SOTC-Full-J and SOTC-Full-En in Table 2.

The amplitude attenuation and phase shift is defined on a single receiving coil while different transmitters are excited.

$$Att_i = Amp_i^{ta}/Amp_i^{tb} \tag{33}$$

$$PS_i = Phase_i^{ta} - Phase_i^{tb} \tag{34}$$

where Att_i is the amplitude attenuation defined on the ith receiver, Amp_i^{ta} and Amp_i^{tb} are the amplitude of the voltage received on the ith receiver when transmitter ta and transmitter tb are excited
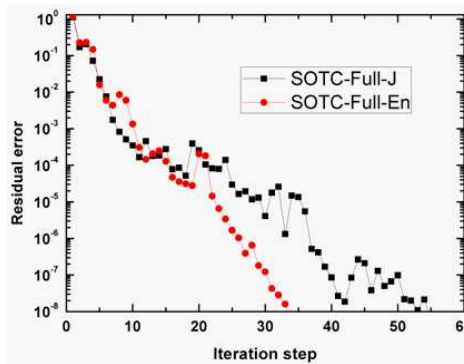
Figure 14. Convergence history of the NC-FEM-DDM using two different TC.

Table 2. Comparison of FEM, NC-FEM-DDM using SOTC-Full-J and SOTC-Full-En.

Step	FEM	SOTC-Full-J	SOTC-Full-En
Unknowns	715948	637977	637977
Reading data	306 s	78 s	78 s
Geo-assembling	19s	12 s	12 s
Filling Matrix	96 s	42 s	42 s
Solving	930 s	482 s	376 s
Memory Cost	23.86 GB	12.3 GB	12.3 GB
Error	-	7×10^{-6}	7×10^{-6}

respectively, and PS_i is the phase shift defined on the ith receiver, $Phase_i^{ta}$ and $Phase_i^{tb}$ are the phase of the voltage received on the ith receiver when transmitter ta and transmitter tb are excited respectively. To illustrate the response of the tool with respect to the conductivity and dielectric parameter, the amplitude attenuation and phase shift of a Z-oriented coil at the transmitter-receiver (T-R) spacings of 0.12 m, 0.2 m, 0.28 m and 0.36 m are given in Fig. 15 and Fig. 16.

From Fig. 15 and Fig. 16, we can conclude that the response of dielectric tool is sensitive to both conductivity and permittivity at 20 MHz. However, the curves of the response with respect to the parameters are completely nonlinear in this case. As a result, it requires lots of research into this kind of instruments in the future so that we can optimize the tool parameters and get a better interpretation of the response.
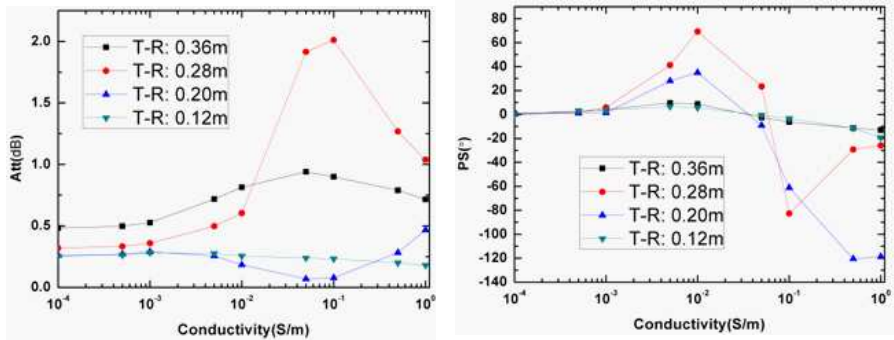
Figure 15. The logging response with respect to the conductivity of the layers.
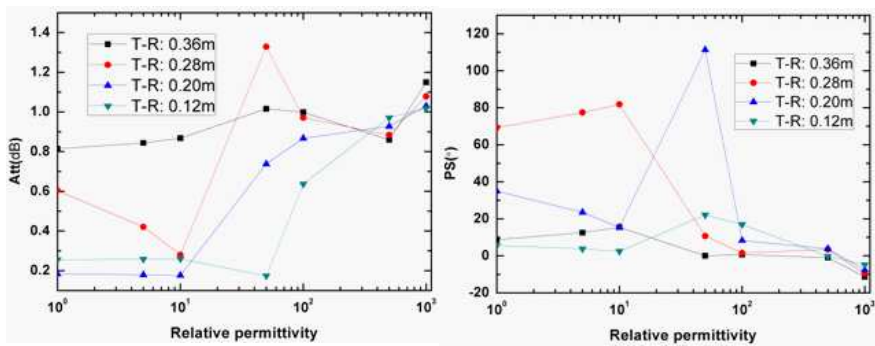
Figure 16. The logging response with respect to the relative permittivity of the layers.

5. CONCLUSION

Numerical modeling of applications both in the high-frequency band and low-frequency band illustrate the advantage of the proposed SOTC-Full-En in this paper. The NC-FEM-DDM developed in this paper using an improved SOTC can significantly alleviate the difficulties for real-life applications. First of all, each subdomain, which may contain arbitrarily shaped structures, has been modeled accurately. Secondly, each non-conformal subdomain is meshed independently, which makes mesh generation easier and permits inconsistency of mesh cells at the interface of subdomains with different scale. Besides, DDM method itself can reduce the memory usage and have high parallel efficiency. Finally, the improved SOTC for DDM has enabled a faster solution by accelerating the iterative convergence. With all the aforementioned advantages, the proposed SOTC-Full-En

in the framework of NC-FEM-DDM has a great potential in dealing with highly sophisticated practical problems in EM applications.

ACKNOWLEDGMENT

REFERENCES

1. Piacentini, A. and N. Rosa, "An improved domain decomposition method for the 3D Helniholtz equation," *Comput. Methods Appl. Mech. Engrg.*, Vol. 162, 113–124., Oct. 1997.

2. Stupfel, B., "A fast-domain decomposition method for the solution of electromagnetic scattering by large objects," *IEEE Transactions on Antennas and Propagation*, Vol. 44, No. 10, 1375–1385, Oct. 1995.

3. Benamou, J. D. and B. Després, "A domain decomposition method for the Helmholtz equation and related optimal control problems," *J. Comput. Phys.*, Vol. 136, 68–82, 1997.

4. Stupfel, B. and M. Mognot, "A domain decomposition method for the vector wave equation," *IEEE Transactions on Antennas and Propagation*, Vol. 48, No. 5, 653–660, May 2000.

5. Vouvakis, M. N., Z. Cendes, and J.-F. Lee, "A FEM domain decomposition method for photonic and electromagnetic band gap structures," *IEEE Transactions on Antennas and Propagation*, Vol. 54, No. 2, 721–733, Feb. 2006.

6. Lee, S.-C., M. N. Vouvakis, and J.-F. Lee, "A non-overlapping domain decomposition method with non-matching grids for modeling large finite antenna arrays," *J. Comput. Phys.*, Vol. 203, 1–21, Feb. 2005.

7. Alonso-Rodriguez, A. and L. Gerardo-Giorda, "New non-overlapping domain decomposition methods for the harmonic Maxwell system," *SIAM J. Sci. Comput.*, Vol. 28, No. 1, 102–122, 2006.

8. Li, Y. and J.-M. Jin, "A vector dual-primal finite element tearing and interconnecting method for solving 3-D large-scale electromagnetic problems," *IEEE Transactions on Antennas and Propagation*, Vol. 54, No. 10, 3000–3009, Oct. 2006.

9. Zhao, K., V. Rawat, S.-C. Lee, and J.-F. Lee, "A domain decomposition method with nonconformal meshes for finite

periodic and semi-periodic structures," *IEEE Transactions on Antennas and Propagation*, Vol. 55, No. 9, 2559–2570, Sep. 2007.

10. Vouvakis, M. N., K. Zhao, S. M. Seo, and J.-F. Lee, "A domain decomposition approach for nonconformal couplings between finite and boundary elements for unbounded electromagnetic problems in R3," *J. Comput. Phys.*, Vol. 225, No. 1, 975–994, Jul. 2007.

11. Li, Y.-J. and J.-M. Jin, "A new dual-primal domain decomposition approach for finite element simulation of 3-D large-scale electromagnetic problems," *IEEE Transactions on Antennas and Propagation*, Vol. 55, No. 10, 2803–2810, 2007.

12. Zhao, K., V. Rawat, S.-C. Lee, and J.-F. Lee, "A domain decomposition method with nonconformal meshes for finite periodic and semi-periodic structures," *IEEE Transactions on Antennas and Propagation*, Vol. 55, No. 9, 2559–2570, 2007.

13. Peng, Z., V. Rawat, and J. F. Lee, "One way domain decomposition method with second-order transmission conditions for solving electromagnetic wave problems," *J. Comput. Phys.*, Vol. 229, No. 4, 1181–1197, 2010.

14. Peng, Z. and J. F. Lee, "Nonconformal domain decomposition method with second-order transmission conditions for time-harmonic electromagnetic," *J. Comput. Phys.*, Vol. 229, 5615–5629, 2010.

15. Fernandez-Recio, R., L. E. Garcia-Castillo, S. Llorente-Romano, and I. Gomez-Revuelto, "Convergence study of a non-standard schwarz domain decomposition method for finite element mesh truncation in electro-magnetics," *Progress In Electromagnetics Research*, Vol. 120, 439–457, 2011.

16. Fotyga, G., K. Nyka, and M. Mrozowski, "Efficient model order reduction for FEM analysis of waveguide structures and resonators," *Progress In Electromagnetics Research*, Vol. 127, 277–295, 2012.

17. Guillod, T., F. Kehl, and C. V. Hafner, "FEM-based method for the simulation of dielectric waveguide grating biosensors," *Progress In Electromagnetics Research*, Vol. 137, 565–583, 2013.

18. Hizem, M., H. Budan, B. Deville, O. Faivre, L. Mosse, and M. Simon, "Dielectric dispersion: A new wireline petrophysical measurement," *Society of Petroleum Engineers*, 116130, 2008.

19. Jin, J. M., *The Finite Element Method in Electromagnetics*, 2nd Edition, Wiley, Hoboken, NJ, 2002.

20. Jin, J. M. and D. J. Riley, *Finite Element Analysis of Antennas and Arrays*, Wiley, Hoboken, NJ, 2009.